High temperature oxidation resistance and thermodynamic properties of (TaNbZr)N and (TaNbZr)C quaternary ceramic coating

Haiyang Yu [a], Wenping Liang [a], Qiang Miao [a], Mengjuan Yin [a], Yong Wang [b c], Hongfei Liu [d], Hongmei Jin [e], Fengxia Wei [d], Na Gong [d]

[a] College of Materials Science and Technology, Nanjing University of Aeronautics and Astronautics, Nanjing 211106, China

[b] School of Materials Science and Engineering, Nanyang Technological University, 50 Nanyang Avenue, Singapore 639798, Singapore

[c] Singapore Centre for 3D Printing, Nanyang Technological University, 50 Nanyang Avenue, Singapore 639798, Singapore

[d] Institute of Materials Research and Engineering (IMRE), A*STAR (Agency for Science, Technology and Research), 2 Fusionopolis Way, Singapore 138634, Singapore

[e] Institute of High Performance Computing (IHPC)), A*STAR (Agency for Science, Technology and Research), 1 Fusionopolis Way, Singapore 138632, Singapore

Abstract

A TaNbZr-based quaternary ceramic coating with a metallurgical transition layer on a titanium alloy surface has been produced. The quaternary ceramic coatings exhibit a face-centered cubic structure and distinct structural orientation. The introduction of carbon and nitrogen significantly improved high-temperature oxidation resistance compared to metallic coatings in cyclic oxidation tests. Specifically, the (TaNbZr)N coating provided effective thermal protection during 800 °C cyclic oxidation for 100 hours (10 cycles). The phase stability and evolution of quaternary ceramic coatings were clarified using in-situ XRD. Further, first-principles calculations elucidated the enhanced thermal stability and high-temperature performance of (TaNbZr)N and (TaNbZr)C coatings.

Graphical Abstract

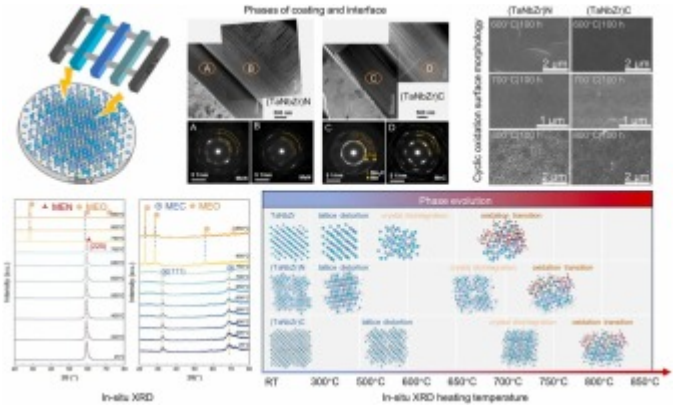

1. Download: Download high-res image (296KB)
2. Download: Download full-size image

- Previous article in issue
- Next article in issue

Keywords
DGPSA
Medium entropy alloys
TaNbZr-based coatings
High temperature oxidation
Thermodynamic stability

1. Introduction

The IVB, VB, and VIB group transition metal nitrides and carbides, known for their high melting points, superior hardness, exceptional wear resistance, excellent high-temperature stability, and resistance to ablation, have been widely employed as wear-resistant coatings and thermal protection coatings in aerospace, marine technology or military industry [1]. Among the extensively studied compounds are binary nitrides and binary carbides such as MN and MC (M=Ti, Zr, Ta, Nb, Hf, etc.), as well as the important and well-established ternary nitrides like TiAlN, CrAlN [2], and the emerging TiZrN, ZrTaN [3], [4]. In recent years, the advent of the concept of multi-principal element alloys has led to the development of numerous novel alloy materials [5], [6]. Multi-principal element alloys typically refer to a class of materials that contain three or more principal alloying elements, showcasing unique characteristics such as lattice distortion [7], sluggish diffusion [8], high entropy effects [9], and cocktail effects [10].

Medium entropy alloys (MEAs) and high entropy alloys (HEAs) represent important constituents of multi-principal element alloys. By fine-tuning composition, elemental content, and manufacturing processes, researchers have endowed them with exceptional mechanical properties and high-temperature stability. Current research indicates that medium-entropy alloys derived from refractory high-entropy alloys, such as NbZrTi, and NbZrTi-based refractory materials, demonstrate exceptional excellent room-temperature ductility and impressive mechanical strength at elevate temperature [11], [12]. Luo et al. [13] proposed a strategy for achieving excellent wear resistance through the in-situ formation of an amorphous crystalline nanocomposite layer and gradient nanostructure in complex TaMoNb alloy films during high-temperature wear. A similar high-temperature wear-resistant strategy was also found in ZrTaNb nitride coatings [14]. Despite the positive influence of multi-element solid solution and entropy stabilization on material properties, the constituent elements continue to wield significant influence over performance aspects, including resistance to oxidation [15]. For instance, Ta, Nb, and Zr have good solubility in Ti, while Mo oxides are volatile at high temperatures, Ta exhibits superior oxidation resistance compared to Zr, and the addition of Nb promotes a denser structure and lower oxide melting temperatures [16], [17], [18]. Additionally, introducing interstitial elements like C, N, O, and B in both HEAs and MEAs can significantly enhance hardness and elastic modulus [19], [20], [21]. Extensive literature suggests that compound coatings of medium/high-entropy alloys manifest heightened hardness and modulus, especially when formed by ceramic layers containing strong nitride or carbide-forming elements [22]. Thus far, various attempts have been undertaken to develop coatings that offer for superior mechanical and high-temperature performance. However, ceramic coatings generally exhibit notable differences in thermophysical properties compared to metal substrates, resulting in challenges a series of adhesion issues like coating cracking due to poor adhesion. To address these issues, diverse methods have been developed, including multi-component alloying [18], multilayering [23], interface coherent strain tuning [24], nanocrystalline structures [25], and gradient layers, to enhance the thermal stability of coatings. One notable preparation technique is the Double Glow Plasma Surface

Alloying (DGPSA), employed for the production of gradient metal or ceramic coatings with a gradually changing composition across the cross-section. DGPSA technology presents substantial advantages in the preparation of nanocrystalline coatings, gradient coatings, and the formation of robust metallurgical bonds [26], [27], [28]. In prior investigations [14], multi-principal element carbide and nitride coatings metallurgically bonded to a titanium alloy substrate were successfully prepared using DGPSA technique. Notably, the TaNbZrN coating, when subjected to high-temperature friction at 500 °C, exhibited a surface with an amorphous-nanocrystalline composite gradient structure, significantly enhancing its high-temperature wear resistance. However, these studies primarily focused on the mechanical properties of coatings, with limited reports on their oxidation resistance and thermal stability. Generally speaking, Ta, Nb, and Zr are not the preferred elements for alloy oxidation resistance, despite being strong nitride/carbide forming elements and having potential entropy-induced enhancements. Therefore, it is necessary and meaningful to continue researching the thermal stability and high-temperature oxidation resistance of these coatings.

For materials used in high-temperature applications, elevated temperatures can cause expansion due to inherent lattice changes, void formation, and phase transitions. Mismatched thermal expansion coefficients result in stress generation at interfaces. Hence, it is crucial in material design to understand thermal expansion to enhance adhesion to substrates and maximize resistance against thermal stress. Measurements of thermal expansion also provide valuable insights into the role of crystal lattice vibrations, lattice defects in thermal properties, as well as phase transitions and non-harmonic mechanisms [29]. While these insights hold theoretical significance, direct measurements may be challenging. With the rapid development of materials computational science, first-principles calculations based on density functional theory plays a pivotal role in predicting intrinsic properties like the formation and stability of new materials, serving as a robust tool in the study of material structure and properties.

In this study, we expanded upon previous research by depositing medium-entropy alloy, carbide, and nitride coatings on a titanium alloy substrate using double glow plasma surface alloying. We investigated the cyclic oxidation kinetics of these coatings within the temperature range of 700–800 °C. Additionally, we conducted in-situ X-ray diffraction (XRD) tests to reveal the structural changes and phase transitions of the coatings. Utilizing experimental findings, we conducted a comprehensive comparative study of the thermodynamic properties of the three coatings using ab initio calculations and a quasi-harmonic Debye-Grüneisen model. Extensive discussions were undertaken to elucidate the high-temperature performance and thermal stability of the coatings. This research offers valuable reference and guidance for the design and application of innovative multi-principal element transition metal ceramic coatings.

2. Theoretical and experimental methods

2.1. Preparation of quaternary ceramic coatings

The matrix material used was TA15 alloy with a nominal composition of Ti-6.5Al-2Zr-1Mo-1 V. Samples were cut into dimensions of 15×15×5 mm^3 using wire cutting. Subsequently, the surfaces were grinded with SiC paper and polished using a Cr_2O_3 suspension, followed by ultrasonic cleaning in a 95 % ethanol solution to remove surface contaminants. The coatings were prepared by double-cathode glow plasma surface alloying furnace. The target was composed of pure metal sheets (Zr, Ta, Nb) and graphite sheets (Fig. 1a), arranged in a regular array with approximately a spacing of 10 mm. The matrix was placed on the cathode worktable below the target, maintaining a distance of about 15 mm from the target. Before depositing the coating, the chamber air was pumped out, cleaned

repeatedly with pure argon to lower than 0.1 Pa, and then the target and workpiece were pre-etched 20 min in pure argon of 20 Pa. Various types of quaternary ceramic coatings were deposited under varying sputtering environments, including low-pressure pure argon or argon-nitrogen mixture atmospheres. Specifically, (TaNbZr)N (MEN), (TaNbZr)C (MEC), TaNbZr (MEA) coatings were deposited on the surface of titanium alloy. MEA and MEC coatings were prepared in pure argon with an argon flow of 100 sccm, while MEN was prepared in an argon nitrogen mixture with an argon flow of 70 sccm and a nitrogen flow of 30 sccm. The working pressure was stable at 20 Pa, the cathodic DC bias voltages of 400 V and 800 V were applied to the target and substrate and the deposition time was 4 h.

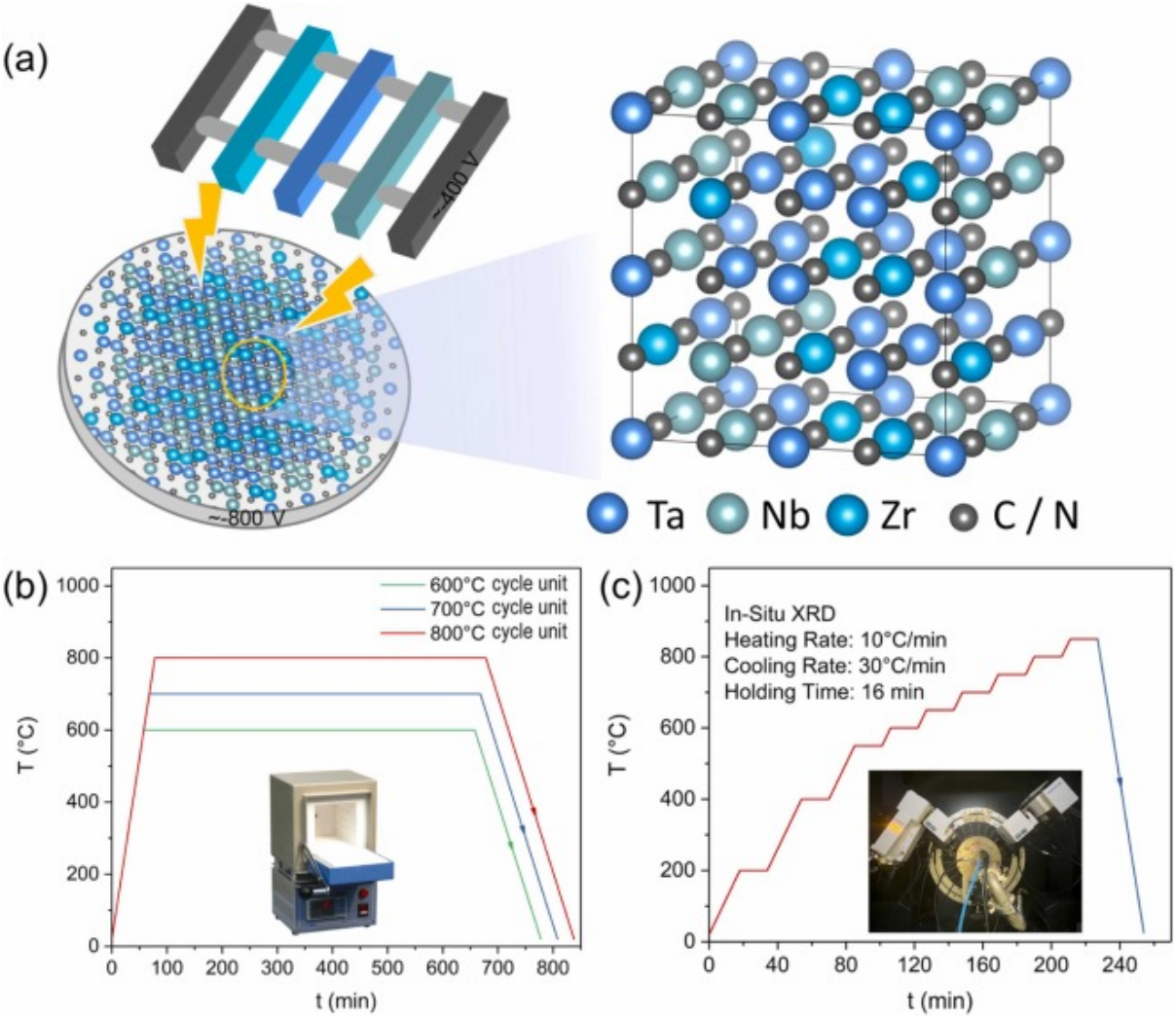

1. Download: Download high-res image (490KB)
2. Download: Download full-size image

Fig. 1. Equipment structure schematic diagram and test process diagram. (a) Target structure diagram with an inset illustration of the crystal structure of SQS supercell. Heating and cooling curves of thermal cycle oxidation test (b) and in-situ XRD test (c) carried out in inserted schematic image.

2.2. High temperature cyclic oxidation test

The thermal cycling oxidation test was carried out under static air at atmospheric pressure within a box furnace (KSL-1100X-S). The non-coated surfaces of the three coating samples were encapsulated with alumina sheets and individually placed in alumina crucibles for pre-weighing before initiating the cyclic oxidation experiments. Each thermal oxidation cycle involved heating from room temperature

to the designated temperature at a rate of 10 °C per minute, followed by a 10-hour exposure at the elevated temperature, and finally cooling to room temperature in air (as illustrated in Fig. 1b). After each cycle, weight changes of the samples were measured using an analytical balance with a precision of 0.1 mg.

2.3. Characterization

The cross-sectional morphology and elemental composition distribution of the coatings were characterized using a scanning electron microscope (SEM) equipped with energy-dispersive X-ray spectroscopy (EDS). X-ray diffraction (XRD) analysis was performed using CuKα radiation source (λ=0.154 nm) to elucidate the crystalline structure of the initially deposited coatings. The scan angle ranged from 30° to 90°, with a step size of 0.02°. The XRD instrument operated at a voltage of 45 kV and a current of 40 mA.

To analyze the dependence of structural characteristics of the coatings on heating temperature, in-situ high-temperature X-ray diffraction analysis was conducted using a D8-Advance Bruker diffractometer equipped with CuKα radiation (λ=1.5406 Å). The three types of coatings were subjected to a heating process that started from room temperature and increased to 850 °C at a rate of 10 °C per minute, followed by cooling at a rate of 30 °C per minute. The detailed heating process is depicted in Fig. 1c. The scanning was performed for 15 minutes with the equilibration time for 1 minute at each selected temperature (room temperature (RT), 200, 400, 550, 600, 650, 700, 750, 800, and 850 °C), covering an angular range of 20° to 80° with a step size of 0.02°.

2.4. The ab-initio calculation details

In this study, the chemical disordered structures in the three coatings were generated using a specialized quasi-random structure (SQS) method [30]. The notable advantage of employing the SQS method lies in its ability to emulate random alloys with a relatively small supercell. The SQS supercells were constructed using the Alloy Theoretic Automated Toolkit (ATAT) code. For the face-centered cubic structures of (TaNbZr)N and (TaNbZr)C, a 64-atom random structure supercell was generated, in which the transition metal atoms randomly occupied the 4a site (0, 0, 0), while non-metallic atoms occupied the 4b positions (1/2, 1/2, 1/2). As for the body-centered cubic structure of TaNbZr, metal atoms randomly occupy the Wyckoff positions 2a site (0, 0, 0) within a 16-atom supercell, as shown in the Fig. 1a.

The calculations were performed using the Vienna Ab initio Simulation Package (VASP) software based on density functional theory (DFT). The exchange-correlation functional employed the generalized gradient approximation in the Perdew-Burke-Ernzerhof form (GGA-PBE). The projector augmented wave (PAW) pseudopotentials were used to describe the energy of the ionic cores and valence electrons. For structural optimization and energy calculations, a plane-wave cutoff energy of 500 eV and a $2\pi \times 1/50$ $Å^{-1}$ k-mesh grid were used. The electronic energy convergence criterion was set at 10^{-5} eV, and the ionic force convergence criterion was 0.015 eV/Å.

The study of thermodynamic properties was carried out using the Debye-Grueneisen model implemented in the GIBBS2 program [31], [32]. The derived equation of state (EOS) at ground state from VASP calculations served as an input data for the model, providing the necessary equilibrium volume, bulk modulus, and other essential values. The Helmholtz energy (F), associated with temperature (T) and volume (V), including the electronic total energy (E_{tot}) calculated from first principles at T = 0 K, the vibrational lattice free energy (F_{vib}), and contributions from electronic thermal excitation (F_{el}), is expressed as a Eq. (1) [33]:(1)F(V,T)=Etot+Fvib(V,T)+Fel(V,T)

When calculating the Helmholtz energy, a critical consideration lies in accurately describing the

vibrational free energy. This study employs the Debye-Grüneisen model to capture the dynamics of lattice vibration and elucidate non-harmonic effects. The computational approach is outlined as follows [29], [34]:(2)Fvib(V,T)=Evib(V,T)−TSvib(V,T)=98kBΘD+kBT[3ln(1−e−ΘD/T)−D(ΘDT)]

Here, kBrepresents the Boltzmann constant, D(ΘD/T) denotes the Debye function computed via numerical methods. Note that the Debye temperature (Θ_D) is a function of volume to incorporate anharmonic effects and the Grüneisen parameter. Combined with the total energy curve obtained from first-principles calculations, the following relationship can be derived [29]:(3)γ(V)=−∂lnΘD∂lnV

Thus, once the equilibrium volume is established, a range of thermodynamic parameters can be derived, such as heat capacity, entropy, and other thermodynamic properties.

3. Results

3.1. Microstructure of as-deposited coatings

Fig. 2 shows the cross-sectional morphologies using back scattered electron (BSE) imaging, accompanied by local EDS mapping of different coatings under identical deposition conditions. The coating of each sample exhibits a dense and uniform structure, free from any noticeable voids or cracks. MEN and MEC coatings exhibit similar thicknesses (about 8.92 μm and 9.04 μm, respectively), which are approximately half the thickness of the MEA coating (about 23.45 μm).This variation in coating thickness is attributed to its dependence on the sputtering yield of the target. The introduction of nitrogen and carbon results in the formation of some compounds on the surface of the target, thereby reducing the sputtering rate [35], [36], [37]. In addition, an obvious 1–2 μm interlayer is evident between the coatings and the substrate. This interlayer arises due to the pre-sputtering process and the initial instability of sputtering composition during the early stages of coating deposition. The chemical composition of each region in Fig. 2 can be found in Table A1 in the Appendix, which shows that the atomic proportion of non-metallic N and C decreases gradually in the deposition layer, the intermediate layer and the substrate, while the matrix element Ti is on the contrary. In addition, a fused bonding layer is observed between the metal coating and the substrate surface, which is a typical characteristic of interface interdiffusion prepared by DGPSA.

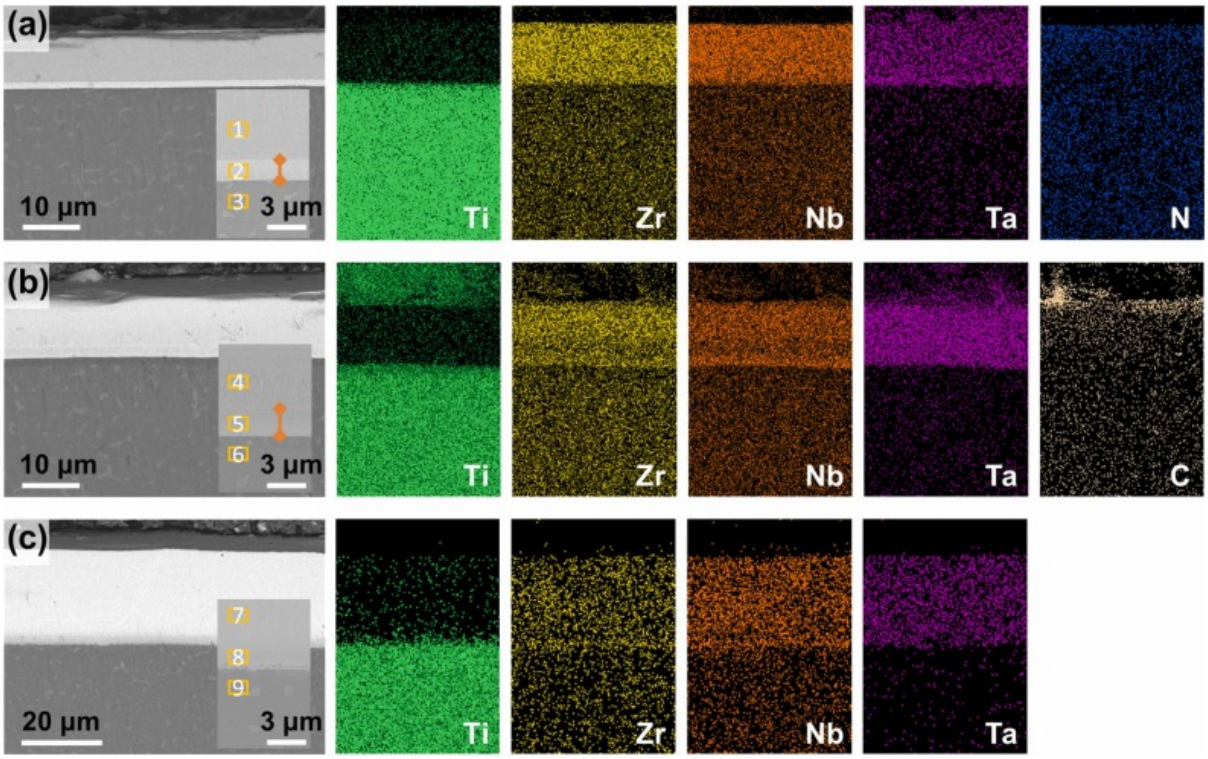

1. Download: Download high-res image (1MB)
2. Download: Download full-size image

Fig. 2. BSE morphology and EDS mapping of coating cross section. (a) MEN, (b) MEC, (c) MEA. The inset is an enlarged image of the interface between the coating and the substrate.

Fig. 3a-c depict the X-ray diffraction spectra of three types of coatings. Both MEN and MEC coatings adopt a face-centered cubic structure, aligning with the structural characteristics of common binary nitrides or carbides. In contrast, the MEA coating exhibits a body-centered cubic structure, primarily attributed to the arrangement of its constituent elements, Ta and Nb, in a body-centered cubic configuration [9]. Moreover, a notable feature distinguishing the coatings produced through DGPSA from conventional metallurgical methods [38], [39], [40], is their pronounced orientation. As elucidated in prior references [41], this alignment is influenced by factors such as bias, temperature, and composition, all of which play pivotal roles in shaping the growth orientation and properties of the coatings [42], [43], [44], [45]. It can be seen that the MEA coating grows preferentially in the [211] direction, whereas the introduction of carbon results in an apparent [111] orientation, and the introduction of nitrogen leads a more distinct [220] orientation.

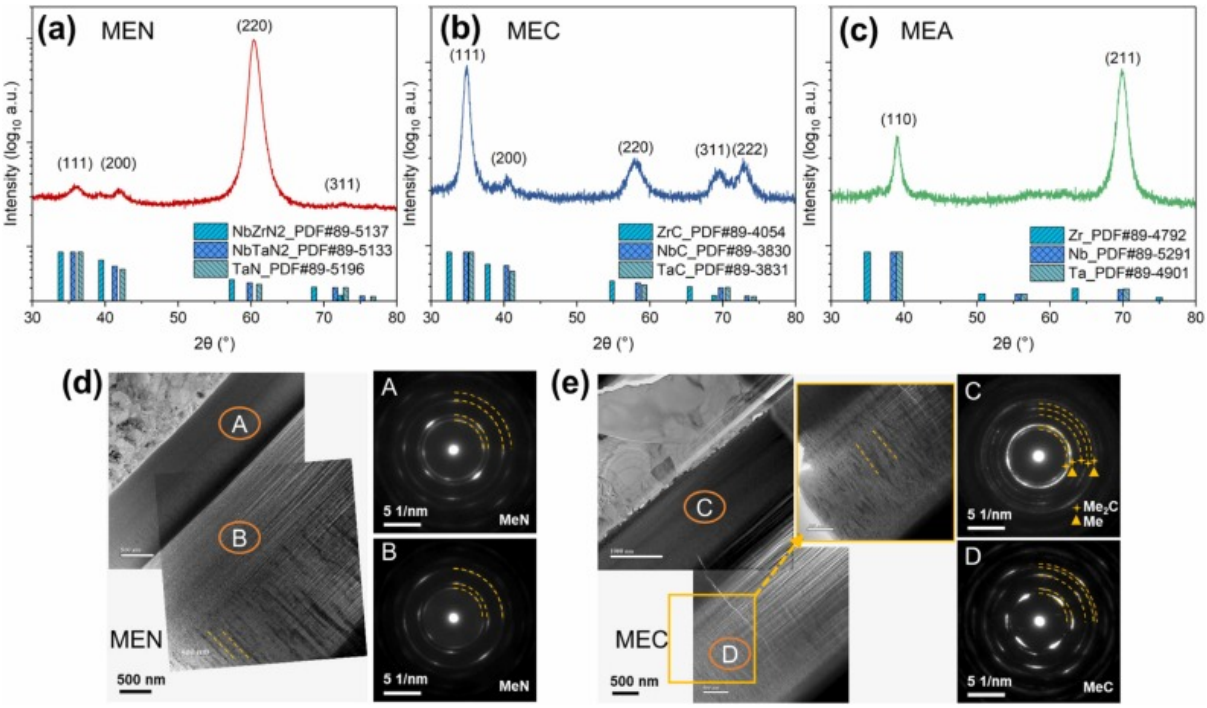

1. Download: Download high-res image (468KB)
2. Download: Download full-size image

Fig. 3. XRD diffraction pattern and TEM studies with SAED pattern of different coatings and interfaces.

As shown in Fig. 3d-e, detailed cross-sectional selected area electron diffraction (SAED) analyses were performed on the intermediate layers in MEN and MEC. The analysis reveals that the intermediate transition layer of the MEC coating primarily comprises subcarbide (Me_2C) and metals (Me). Similarly, the intermediate transition layer of the MEN coating is predominantly composed of MeN. This is attributed to atomic diffusion during the thermal deposition process of the coatings, where nitrogen or carbon atoms diffuse inward, gradually forming the respective carbides (or nitrides) and subcarbides (or subnitrides). Furthermore, TEM images of the MEC and MEN outer layers reveal some nano-scale stripe-like crystalline columns. The selected area electron diffraction (SAED) patterns (bright spots) also exhibit a single-phase face-centered cubic structure with a clear preferred

orientation, consistent with the previous X-ray diffraction results. The growth direction of the nano-crystalline columns in the outer layer of MEN is mostly parallel, while MEC exhibits varying angles between the columns. This observation is consistent with the pole figure measurements reported in the previous work [41].

3.2. Cyclic oxidation test at different temperatures in air

Fig. 4 shows the mass gain curve of the coating during cyclic oxidation at 600 °C, 700 °C and 800 °C for 100 h (10 cycles). Here, the mass gain was defined as the mass change per unit area corresponding to the deposited coating after oxidation.

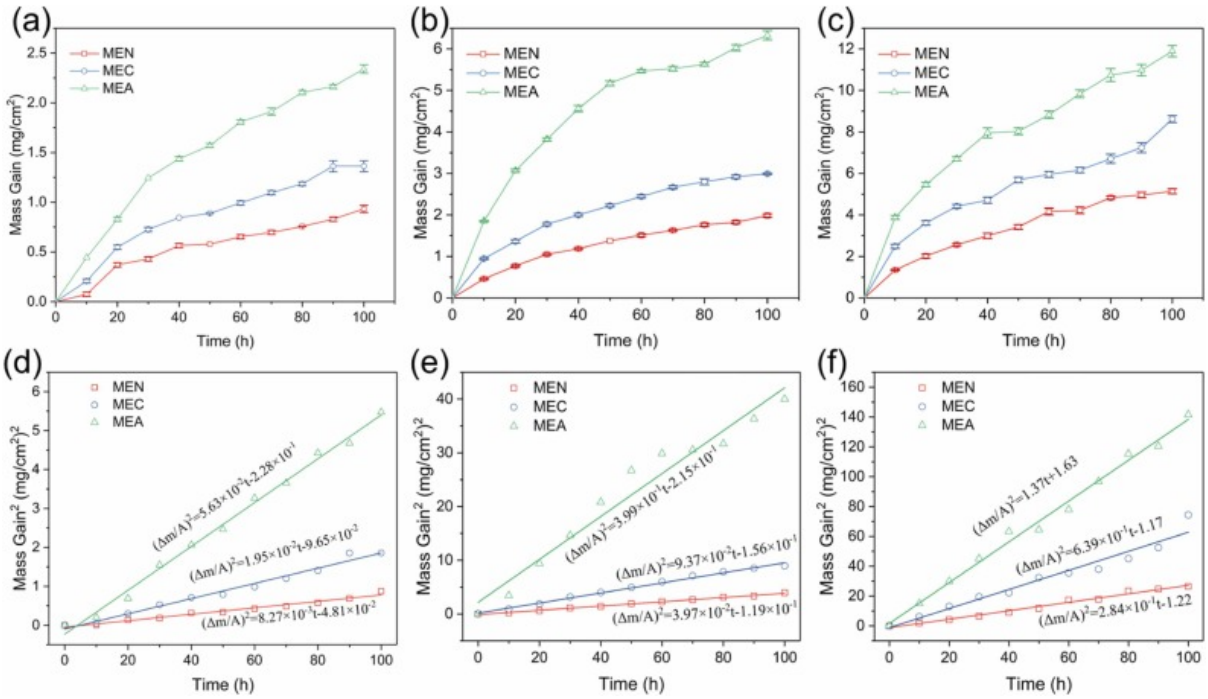

1. Download: Download high-res image (366KB)
2. Download: Download full-size image

Fig. 4. Thermogravimetric curves (a, b, c) and the $(\Delta m/S)^2$ versus time curves (d, e, f) of MEN, MEC and MEA coatings after cyclic oxidation in air at 600 °C (a, d), 700 °C (b, e) and 800 °C (c, f).

As shown in Fig. 4a-c, it is evident that the mass gain of all coatings increases with the elevated oxidation temperature. Throughout all temperatures, the mass gain of MEN and MEC coatings consistently remains lower than that of MEA coatings, underscoring the superior thermal stability provided by ceramic coatings. It can be observed that in the initial stage of Fig. 4a, the mass gain of the ceramic coating is minimal during the initial stages of exposure, indicating that the coating undergoes a slow transition oxidation phase. This suggests that the coating forms a protective oxide layer that can effectively hinder further oxidation, thereby maintaining good stability for a short duration at this temperature. Subsequently, there is a rapid increase in mass followed by a gradual slow down in the growth rate. The swift increase in mass is generally related to the structural transformation of the coating, the chemical reaction, or the fracture of the initial protective layer. As temperature rises and time progresses (see Fig. 4b and c), the slow increase in the coating mass gain is attributed to the formation of a new protective oxide layer.

The oxidation process curves of the three coatings basically conform to the parabolic, indicating that the oxidation rate of coatings obeys the law of diffusion control. The parabolic oxidation rate can be described by Eq. (4).(4)(ΔmS)2=kt+cWhere Δm and S refer to the mass change and the sample

surface area, t represent the oxidation time, k and c are constants related to oxidation kinetics.

Fig. 4d-f shows the $(\Delta m/S)^2$ versus time curves of three coatings at 600 °C, 700 °C and 800 °C. Best-fitting straight lines were obtained with coefficient of determination R^2 in the Table A2. The activation energy of the coating can be calculated based on Arrhenius equation (Eq. (5)). Here, A0 and Ea represent the Arrhenius constant and activation energy respectively. R is the gas constant (about 8.314 $J \cdot mol^{-1} \cdot K^{-1}$)) and T is the absolute temperature. Through logarithmic operation, Eq. 5 is transformed into Eq. 6, and the ln*k* against 1/*T* curves can determine the activation energy.(5)k=A0exp(−EaRT)(6)lnk=lnA0−EaRT

Fig. 5 shows the variation of ln*k* and 1000/*T* across all coatings. By conducting data fitting and subsequent calculations, the activation energies for the MEN, MEC and MEA coatings have been determined to be 136.9 kJ/mol, 134.7 kJ/mol and 124.7 kJ/mol, respectively. Obviously, compared with MEA coatings, MEN and MEC coatings show higher activation energy, indicating enhanced thermal stability. The thermal stability of the coating reflects its high temperature performance to a certain extent.

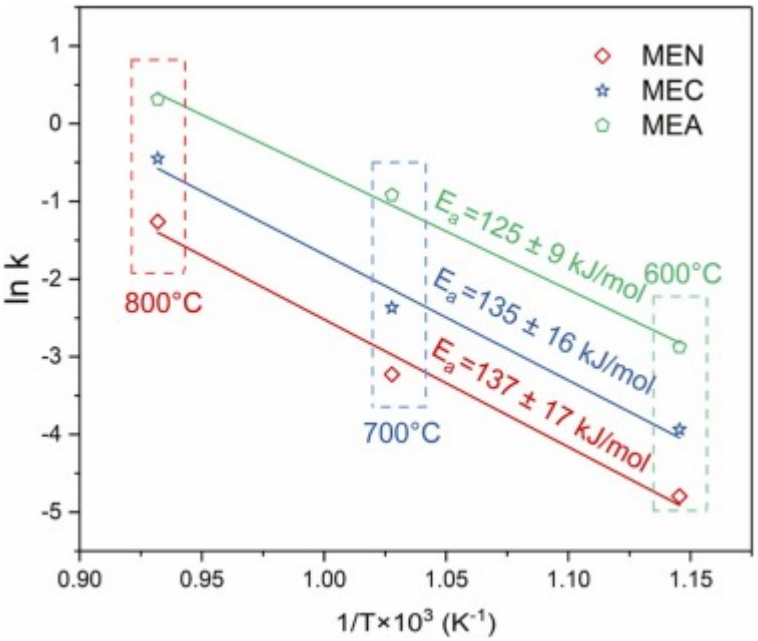

1. Download: Download high-res image (127KB)
2. Download: Download full-size image

Fig. 5. The Arrhenius curves of three coatings after cyclic oxidation in air at 600 °C, 700 °C and 800 °C.

To enhance the visual representation of the coating's oxidation process, distinct analyses were conducted on samples subjected to cyclic oxidation for 1 cycle and 10 cycles at various temperatures. The dynamic mechanism of oxidation process is further revealed by the morphology of oxidation surface and the thickness of oxide layer at different time scales.

Fig. 6 shows the surface morphology and EDS point composition analysis of the three coatings after oxidation in static air at 600 °C, 700 °C and 800 °C for 1 cycle.

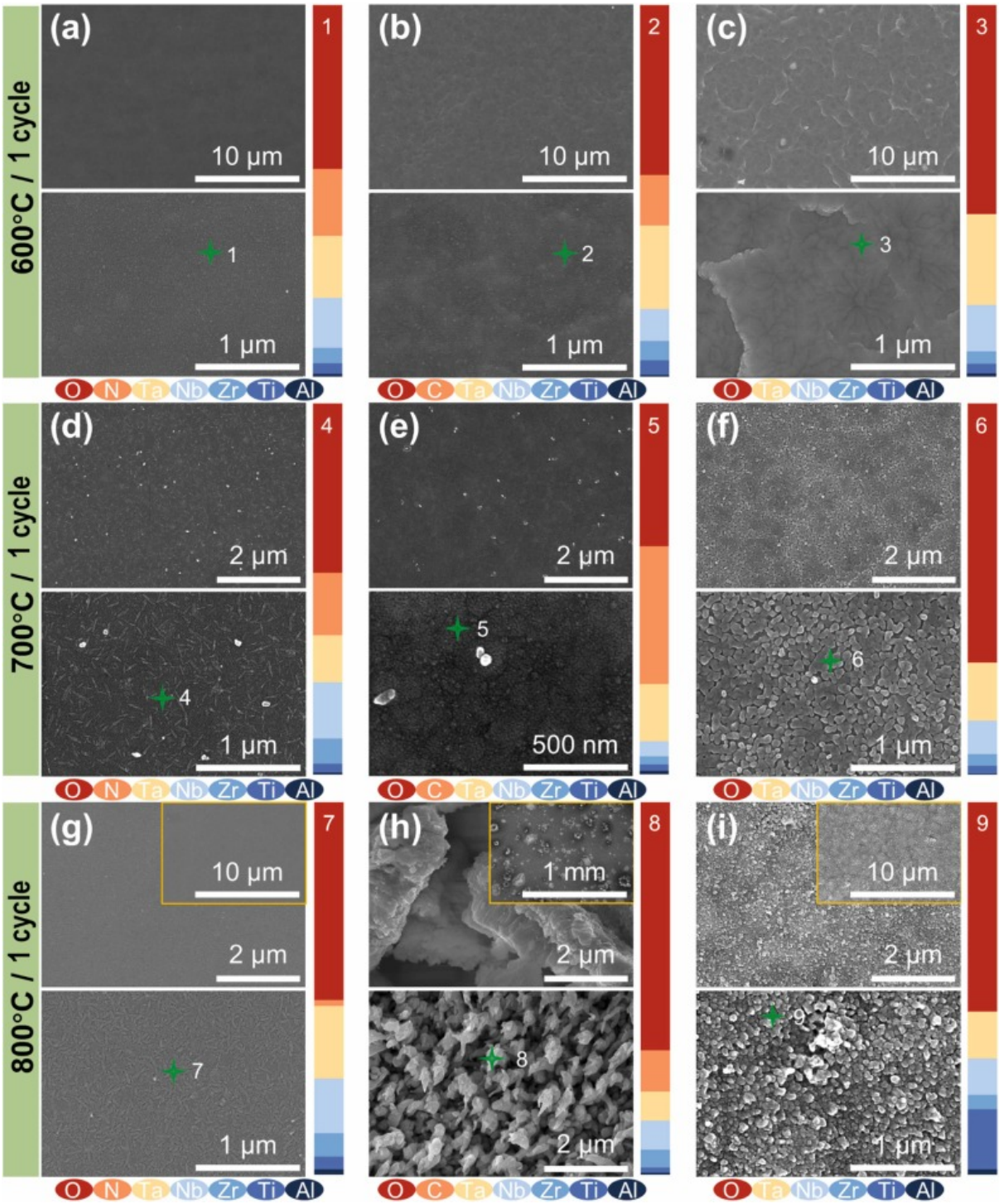

1. Download: Download high-res image (1MB)
2. Download: Download full-size image

Fig. 6. The surface SEM images and corresponding EDS point scanning results of the three coatings after cyclic oxidation in air at 600 °C (a, b, c), 700 °C (d, e, f) and 800 °C (g, h, i) for 1 cycle. (a, d, g) MEN, (b, e, h) MEC, (c, f, i) MEA.

Fig. 6a-c demonstrate the three coatings remain smooth without macroscopic cracks after oxidation at 600 °C for 1 cycle, and there is no apparent coating failure. It is worth noting that many micro-fold scales appears on the surface of the MEA coating. EDS analysis shows that the surface is mainly composed of oxides of the coating composition, with no exposure of the substrate. Fig. 6d-f reveal the

three coatings maintain their flatness after 1 cycle of oxidation at 700 °C, but small white oxide particles appear on the surface. Among them, the MEN coating surface exhibits worm-like patterns. The MEC coating surface shows minimal features except for slight undulations. In contrast, the MEA coating surface forms relatively regular particulate oxides with noticeable pores between particles, which facilitate the diffusion of oxygen. When the three coatings are oxidized at 800 °C for 1 cycle (Fig. 6g-i), surface features become more distinct, and the surface is primarily composed of the corresponding metal oxides. In Fig. 6g, the nitride coating surface remains smooth without macro-cracks, and the worm-like structures increase in quantity, resembling interlocking bamboo leaves. Larger pitted particles appear on the surface of the carbide coating in Fig. 6h, with elongated shapes at their tops and tadpole-like shapes at their bottoms. The oxidized surface in Fig. 6i appears rougher and less smooth compared to the lower temperatures. Aggregated oxide particles form larger grains, and EDS results indicate noticeable diffusion of matrix elements (Ti) to the surface.

Fig. 7 depicts the surface morphology and energy spectrum analysis of the three coatings after oxidation in static air at 600 °C, 700 °C, and 800 °C for 10 cycles. The oxidation results demonstrate that all three coatings maintain their integrity after 10 cycles of oxidation at 600 °C.

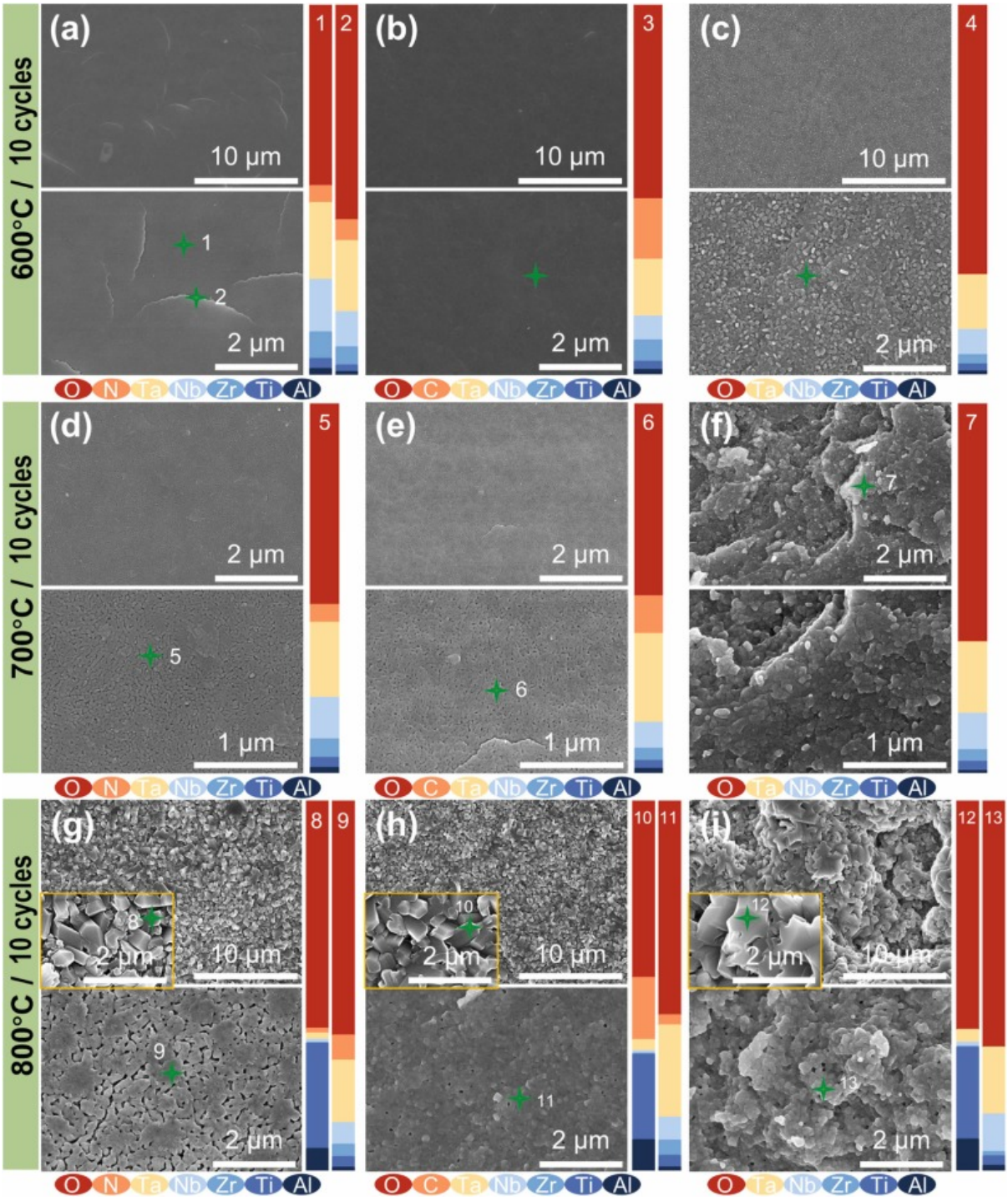

1. Download: Download high-res image (1MB)
2. Download: Download full-size image

Fig. 7. The surface SEM images and corresponding EDS points of the three coatings after cyclic oxidation in air at 600 °C (a, b, c), 700 °C (d, e, f) and 800 °C (g, h, i) for 10 cycles. (a, d, g) MEN, (b, e, h) MEC, (c, f, i) MEA.

As shown in Fig. 7a-c, the surface of the MEN coating exhibits oxygen-rich micro-sized oxidation scales due to localized oxidation under prolonged thermal exposure. Comparatively, the MEC coating displays greater stability, with less observable micro-sized oxidation scales. Conversely, the MEA coating surface showcases numerous small oxide particles, indicating rapid initiation of oxidation

under prolonged exposure at this temperature. After 10 cycles of oxidation at 700 °C (Fig. 7d-f), the MEN and MEC coatings remain mostly intact, presenting worm-like and porous microstructures, respectively. However, the MEA coating exhibits larger oxide scales with a layered peeling pattern. Upon elevating the temperature to 800 °C and subjecting the coatings to 10 cycles of cyclic exposure in a hot air environment, significant delamination is observed on the surfaces of all three coatings. Fig. 7g-i illustrate the microscopic morphology of the delamination areas and the remaining coating surfaces after oxidation. It can be found that the delamination areas of the MEN and MEC coatings share a similar surface morphology characterized by uniformly distributed fine oxide particles, whereas the delamination area of the MEA coating features relatively larger oxide particles. Elemental analysis reveals that the delamination areas of all three coatings are primarily composed of oxidized matrix elements (Ti, Al), with the original coating composition nearly depleted. Additionally, the MEN and MEN coatings maintain a morphology similar to that at 700 °C, although with significantly increased dimensions and porosity in the microstructure, providing further evidence of intensified oxidation.

Fig. 8 illustrates the cross-sectional morphologies of three coatings after oxidation at 600 °C, 700 °C, and 800 °C for 1 cycle and 10 cycles, respectively. The morphologies and thicknesses of the cross-sectional oxide layers contribute to a deeper comprehension of the degree of coating oxidation.

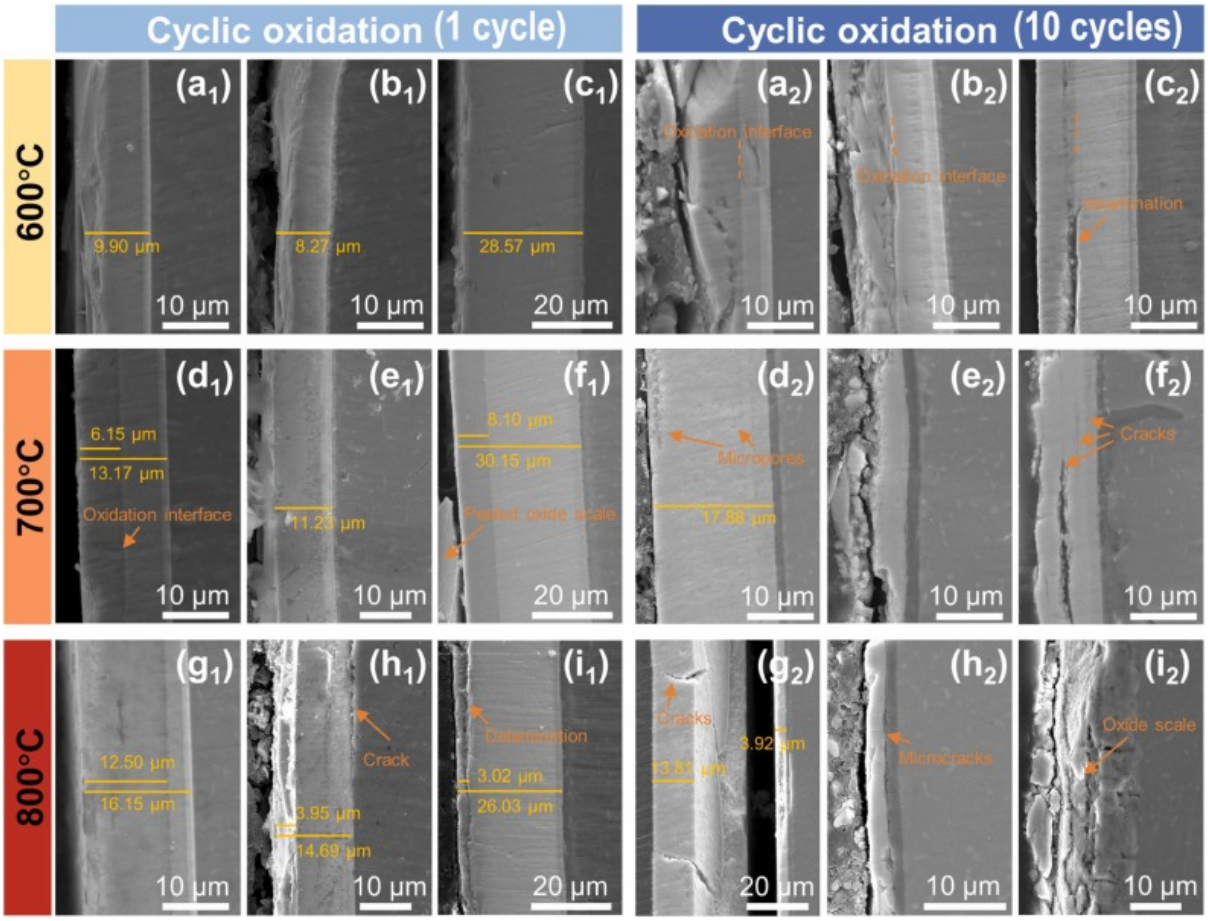

1. Download: Download high-res image (713KB)
2. Download: Download full-size image

Fig. 8. The cross-section morphologies of (a, d, g) MEN coating, (b, e, h) MEC coating, and (c, f, i) MEA coating after oxidation at 600 °C, 700 °C, and 800 °C for 1 cycle and 10 cycles, repectively.

Fig. 8(a_1-i_1) show that after thermal oxidation in static air at different temperatures for 1 cycle, the

thickness of the coatings increased slightly, yet remained predominantly intact. At 600 °C, none of the coatings exhibited pronounced oxide layers. As the temperature increased, distinct oxide layers appeared on the surfaces of the MEN and MEA coatings. Specifically, the oxide layer on the MEN coating surface exhibited a compact, pore-free structure, with a continuous interface. Conversely, the oxide layer on the MEA coating surface displayed delamination phenomena on its surface, and significant interface cracking occurred at 800 °C, confirming the previously mentioned surface morphology. The MEC coating surface exhibited a thin oxide layer only at 800 °C. However, slight cracks were observed at the interface between the coating and the substrate.

After undergoing cyclic oxidation for 10 cycles, all three coatings displayed varying degrees of oxidative erosion. Fig. 8(a_2-i_2) represents the cross-sectional morphologies of the residual coating regions. It should be noted that the specimens underwent mechanical grinding and polishing procedures, which could lead to secondary damage to the oxidized coatings. It can be observed that after 10 cycles of oxidation at 600 °C, the coatings were not fully oxidized; only the surface exhibited an oxide layer. However, at 700 °C and 800 °C, the coatings predominantly transformed into a loose oxide layers with some micropores. The oxide layer on the MEA coating manifested as layered delamination, with noticeable diffusion phenomena occurring at the coating-interface boundary. The oxide layers on the MEN and MEC coatings exhibited gradual thickening as a result of oxidation. Notably, the interface between the oxide and nitride coating appeared smoother compared to that between the oxide and carbide coating, contributing to relatively improved adhesion. The oxide layer formed from the nitride coating exhibited good adhesion to the substrate at elevated temperatures, with no apparent microcracks at the interface. In comparison, the MEN coating showed better resistance to the stepwise delamination seen in the MEA coating, and avoided the brittle separation observed in the MEC coating. Its oxide layer presented a dense and uniform cross-section, effectively covering the surface. The results indicate that further adjustments in coating composition and structural gradients may significantly enhance the adhesion between ceramic coatings and substrates.

3.3. Phase evolution of in situ XRD test

The lattice transformations of various coatings as they underwent temperature changes were studied by in-situ high-temperature X-ray diffraction experiments, which provided a basis for further understanding their thermal stability. As shown in Fig. 9, X-ray diffraction patterns of three different coatings were recorded from room temperature to 850 °C.

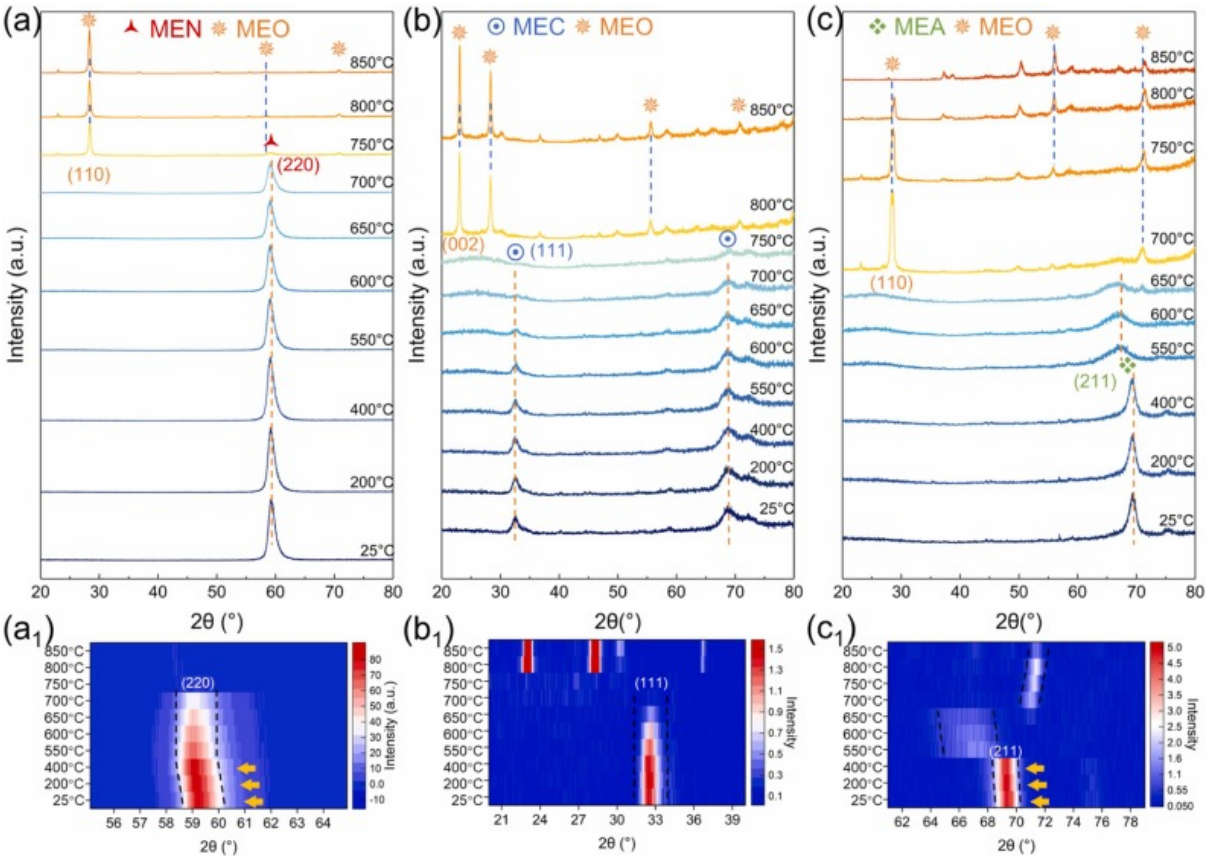

1. Download: Download high-res image (577KB)
2. Download: Download full-size image

Fig. 9. In-situ XRD diffractograms of (a) MEN, (b) MEC and (c) MEA coatings. a_1, b_1 and c_1 are the corresponding contour plots.

For both MEN and MEC coatings (see Fig. 9a and b), it is noteworthy that they maintained stable crystalline structures up to 700 °C and 750 °C, respectively, without the emergence of any new phases. In the XRD pattern of the MEN coating, an original peak with considerable intensity was observed around 59.2°. The intensity of this peak remained constant below 500 °C but gradually decreased as the temperature exceeded 550 °C. This implies that structural changes, such as minor decomposition or lattice relaxation, commenced after 550 °C, causing a reconfiguration of atoms within the crystal lattice and subsequently weakening the diffraction signal. Upon reaching 750 °C, the XRD pattern of the MEN coating exhibited a broadened shoulder around 59.2° and new peaks at angles such as 22.9° and 28.3°, corresponding to major oxide phases which are marked as MEO in Fig. 9, such as Ta_2O_5 (PDF#97–023–6386), Nb_2O_5 (PDF#97–000–1840) and ZrO_2 (PDF#97–001–8190). This indicates that at this temperature, the coating retained only a small amount of the nitride phase and had essentially transformed into the respective oxide phases. It is worth noting that the coating maintained a high-intensity (110) preferred orientation at 850 °C, underscoring the remarkable stability of the oxide phase originating from the nitride phase conversion. The higher intensity might be attributed to the suppression of lattice defects and coarser grain structures at elevated temperatures [46].

In contrast, the thermal stability of the MEC coating was relatively good. The coating retained its crystalline structure below 600 °C, an increase in temperature from 600 °C to 750 °C resulted in a gradual reduction in the intensity of the original crystalline diffraction peak, broadening of the peak,

and the appearance of a broad peak in the low-angle range of 20–30°. These observations suggest an increase in the amorphous phase due to the relaxation and decomposition of the original lattice. At 800 °C, the carbide coating transformed into oxide phases, with a (002) preferred orientation being evident.

Compared to the former two, the thermal stability of the MEA coating was relatively weaker. Upon heating to 550 °C, the intensity of the original crystalline diffraction peak decreased significantly, accompanied by noticeable broadening and low-angle shifts. This indicates that, at this temperature, changes occurred in the atomic arrangement within the lattice due to thermal expansion, resulting in a minor phase transformation. However, at 700 °C, the coating underwent complete transformation into an oxide phase with a (110) preferred orientation. Nevertheless, it is worth noting that, with further temperature increase, such as at 850 °C, the intensity of (110) peak of the oxide phase coating gradually weakened. This suggests that the oxide phase coating derived from the metal phase conversion could not maintain satisfactory stability at this elevated temperature.

3.4. Thermodynamic properties of coatings

Based on the cyclic oxidation test results, it is evident that MEN and MEC exhibit prominent resistance to high-temperature cyclic oxidation. This is closely related to the intrinsic thermodynamic properties of the materials. Therefore, to gain deeper insights into the thermodynamic properties of MEN and MEC within the range of 0–1200 K, a series of thermodynamic parameters were calculated using the quasi-harmonic Debye-Grüneisen model, as illustrated in Fig. 10.

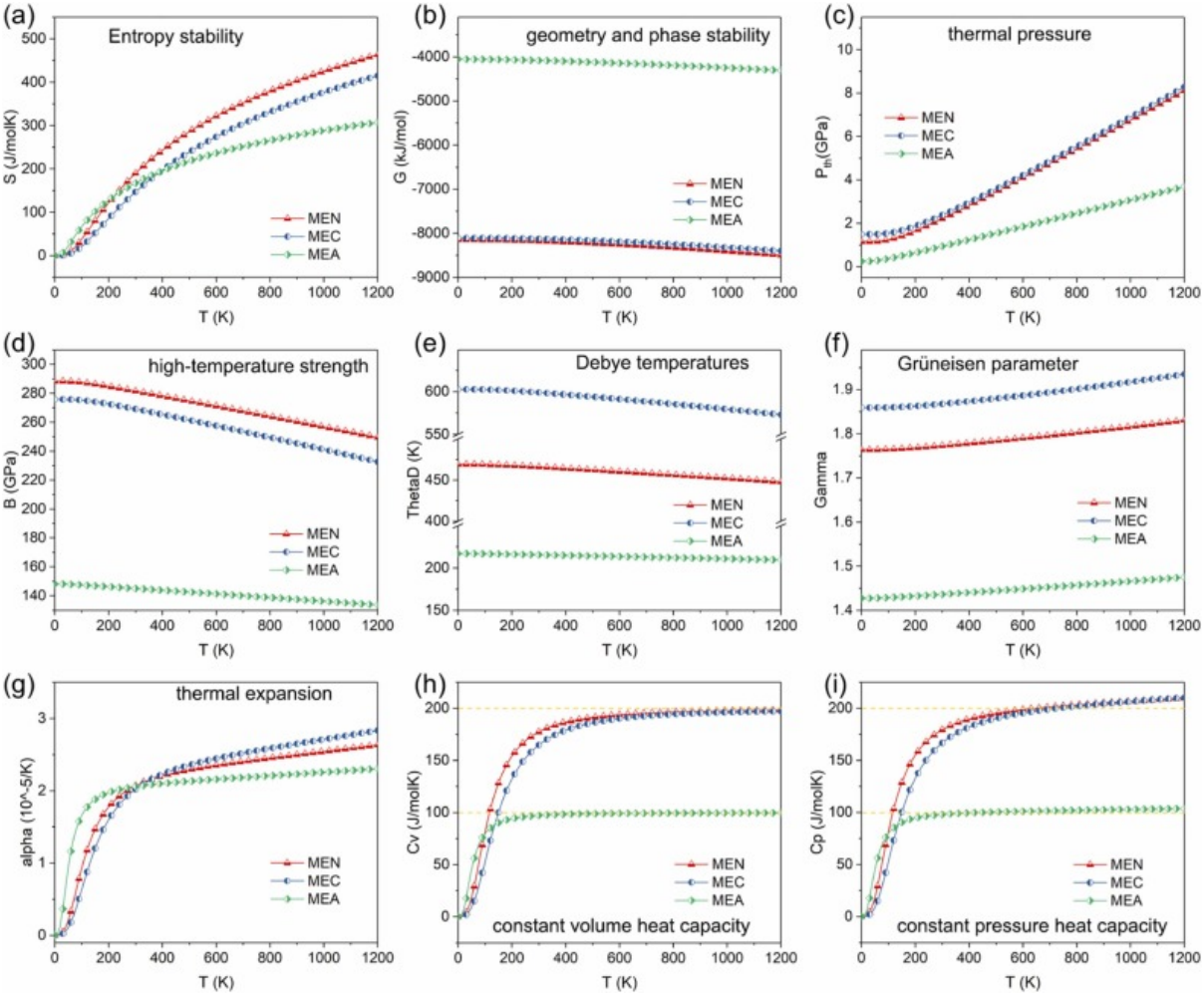

1. Download: Download high-res image (598KB)

2. Download: Download full-size image

Fig. 10. The curves of thermodynamic parameters change with temperature. (a) entropy (*S*), (b) Gibbs free energy (*G*), (c) thermal pressure (P_{th}), (d) bulk modulus (B), (e) Debye temperature (ΘD), (f) Grüneisen parameter (γ), (g) thermal expansion (α), (h) constant volume heat capacity (C_v), and (i) constant pressure heat capacity (C_p).

The entropy calculations for the three coating systems are depicted in the Fig. 10a. The entropy versus temperature curves for MEN and MEC exhibit similar shapes. The entropy of both materials increases with rising temperature, but the rate of increase gradually diminishes. It is evident that the entropy of MEN and MEC is notably higher than that of MEA at high temperatures. This difference might stem from the addition of the non-metallic elements N and C, with the influence of N being more pronounced than that of C. According to the Gibbs free energy criterion, the contribution of -*TS* is more negative, indicating that MEN and MEC might be more stable than MEA at higher temperatures. This is consistent with the variation of the non-equilibrium Gibbs free energy (G*) with temperature under constant pressure conditions, as described in Fig. 10b. The function of the non-equilibrium Gibbs free energy [32], which describes geometry and phase stability, is shown in Eq. 7, where E_{sta} represents the statically calculated energy obtained from first principles, F^*_{vib} represents the non-equilibrium vibrational Helmholtz free energy, and χ includes atomic positions and crystal structure parameters.(7)G*(V;p,T)=Esta(χopt,V)+pV+Fvib*(χopt,V;T)+…

For static-constrained quasi-harmonic approximation, the effect of temperature is expressed through thermal pressure rather than the thermal stress tensor, and the free atomic coordinates are solely determined by the cell volume. Fig. 10c represents the thermal pressure variation in the coatings. It is observable that MEC and MEN coatings exhibit rapid increases in thermal pressure with elevate temperatures compared to the metallic coating (MEA). Especially, MEC coating displays slightly higher thermal pressure, suggesting that carbide and nitride coatings might lead to deformation, stress concentration, or cracking issues more readily than the metallic layer TaNbZr. Therefore, employing a reliable metallic intermediate layer can serve as a method to alleviate these concerns.

In Fig. 10d, the bulk modulus of MEN and MEC exhibits a similar trend, sharply decreasing as the temperature rises. This indicates significant softening for both above 200 K. Additionally, within the same temperature range, the bulk modulus of MEN and MEC is significantly higher than that of MEA. This indicates that MEN and MEC demonstrate superior high-temperature strength, making them more suitable for applications in elevated temperature environments.

Fig. 10e and f illustrates the variations in the Debye temperature and Grüneisen parameter for the three coatings with increasing temperature. It is observed that the Debye temperatures of the three coatings gradually decrease with increasing temperature, yet the overall impact of temperature on the Debye temperature is not significant. The incorporation of non-metallic elements N and C, particularly in MEC, leads to higher Debye temperatures compared to MEA. This implies that the coatings possess higher thermal conductivity, reflective of their greater hardness and melting point due to more intense atomic vibrations within the lattice. Correspondingly, the Grüneisen parameter describes the response of phonons (lattice vibrations) in a solid to changes in pressure and temperature. Higher values of γ usually correspond to higher thermal conductivity and thermal expansion coefficients.

In coating applications, the coefficient of thermal expansion (CTE) of materials stands as a crucial consideration, defining the rate of volume change concerning temperature fluctuations, often determined through the equation α=1V(∂V∂T)p. Disparities in CTE commonly result in coating delamination, cracking, or stress concentration. The calculated thermal expansion coefficients for

the three materials are depicted in Fig. 10g. The CTE of MEN and MEC sharply increases with rising temperatures up to approximately 300 K, followed by a stable trend beyond 300 K. It is evident that the CTE of MEN and MEC surpasses that of MEA at temperatures above 400 K. This indicates that the addition of non-metallic C and N to metallic TaNbZr increases its high-temperature CTE, and the C exhibits a slightly larger impact. In this study, there exists a thin metallic layer between the coating and substrate. Therefore, MEN coating, with a thermal expansion coefficient intermediate between MEA and MEC, is more beneficial to reduce thermal expansion mismatch and is hence more suitable for engineering applications in high-temperature environments.

The heat capacity at constant volume (C_v) reflects the heat absorbed or released by a substance under conditions of constant volume during temperature changes. As shown in Fig. 10h, the C_v values of the three coatings sharply increase at lower temperatures, followed by a gradual rise at higher temperatures, eventually approaching a constant value known as the Dulong-Petit limit, given by Cv=3nR, where *n* is the number of atoms per unit cell [47]. Within the temperature range considered, the C_v value of MEN consistently surpasses that of MEC at the same temperatures, showing less divergence at higher temperatures but more notably at lower temperatures. Additionally, the constant pressure heat capacity (C_p) reflects the heat absorbed or released by a substance under conditions of constant pressure during temperature changes. As depicted in Fig. 10i, the C_p values of the three coatings exhibit a trend similar to C_v with changing temperatures. However, it is worth noting that the C_p values do not converge toward the Dulong-Petit limit of C_v at higher temperatures, consistently maintaining a slightly higher value than the C_v and marginally increasing. This relationship can be clearly understood from the expression: Cp−Cv=(3α)3BTV, where α represents the coefficient of thermal expansion. In summary, within the 0–1000 K range, MEN demonstrates relatively higher heat capacity, potentially indicating better thermal stability in environments with significant temperature fluctuations. However, this increase is not notably pronounced compared to MEC, particularly at temperatures higher than 500 K.

4. Discussion

4.1. Structural and mechanical stability of quaternary ceramic

Table 1 presents the lattice constants of the MEC and MEN coating systems calculated through first-principles at 0 K. It can be observed that the lattice constants for MEC and MEN crystal structures are 4.53 Å and 4.46 Å, respectively, closely matching the values calculated by Vegard's Law [48]. This indicates the reliability of the equilibrium lattice constants obtained from the first-principles calculations for the coating systems. In addition, based on the DFT calculations of the relaxed energy at 0 K, we can analyze that the structural models of the coating are thermodynamically stable. The thermodynamic stability of the coating system can also be assessed by the formation enthalpy ΔH_f [49]:(8)ΔHf=(Etotal−∑NiEi−solid)/∑Ni(i=Ta,Nb,Zr,CorN)

Table 1. Calculated equilibrium lattice constants, DFT energies and formation enthalpy of the different systems at 0 K.

Systems	TaC	NbC	ZrC	Average*	MEC
	4.479	4.482	4.710	4.537	4.532
Lattice constants (Å)	4.479[b]	4.507[b]	4.711[b]	4.544	
	4.446[e]	4.472[e]	4.685[e]	4.512	
Energies (eV/atom)	−11.101	−10.283	−9.738	−10.555	−10.560

Systems	TaC	NbC	ZrC	Average*	MEC
ΔH_f (kJ/mol)	−11.1[b]	−10.12[b]	−9.73[b]	−10.512	
	−55.964	−55.2207	−88.217	−63.841	−64.314
	−54.997[b]	−45.348[b]	−82.013[b]	−59.339	
Systems	**TaN**	**NbN**	**ZrN**	**Average****	**MEN**
Lattice constants (Å)	4.418	4.418	4.597	4.463	4.463
	4.42[c]	4.42[c]	4.6[c]	4.465	
	4.424[d]	4.412[e]	4.576[e]	4.459	
Energies (eV/atom)	−10.9292	−10.2767	−10.1728	−10.577	−10.603
ΔH_f (kJ/mol)	−83.003	−98.262	−173.815	−109.521	−112.027

*
average value estimated by the rule of mixture (TaC, TaC, NbC, ZrC).
**
average value estimated by the rule of mixture (TaN, TaN, NbN, ZrN).
b
[56],
c
[57],
d
[58],
e
[59].

where E_{total} is the total energy of the system, N_i is the number of atoms in the system, and $E_{i\text{-}solid}$ is the energy of per atom in the solid state element. From Table 1, it can be observed that the system binding energy for MEN and MEC is negative, indicating a stable structure [50]. Furthermore, the negative formation enthalpy suggests that the quaternary ceramics are more stable compared to the solid elements, and the introduction of non-metallic nitrogen is more favorable for stability than the introduction of non-metallic carbon.

The crystal structures of MEN and MEC exhibit noticeable lattice distortions. Considering that most physical and chemical properties are related to bonding, the degree of crystal distortion is assessed here by variations in the metal-nonmetal bond lengths. It can be observed that the values of the bond lengths have a normal distribution (Fig. 11a). Additionally, the distribution range of Me-N bond lengths is greater than that of Me-C bond lengths, indicating a greater lattice distortion in MEN. The box-plots with black lines and square marks denote the median and mean values of the bond length values, respectively. It can be seen that the Me-C bond lengths are longer on average than the Me-N bond lengths, suggesting that MEC has larger lattice parameters, consistent with previous results. Therefore, the introduction of nitrogen in medium-entropy metals leads to greater lattice distortion, which has also been verified in the literature [51]. Theoretically, lattice distortion increases hardness, reduces thermal conductivity [52], decreases the temperature dependency of some thermophysical

properties, and can also decrease the intensity of X-ray diffraction peaks, enhancing the thermodynamic stability of the structure [9].

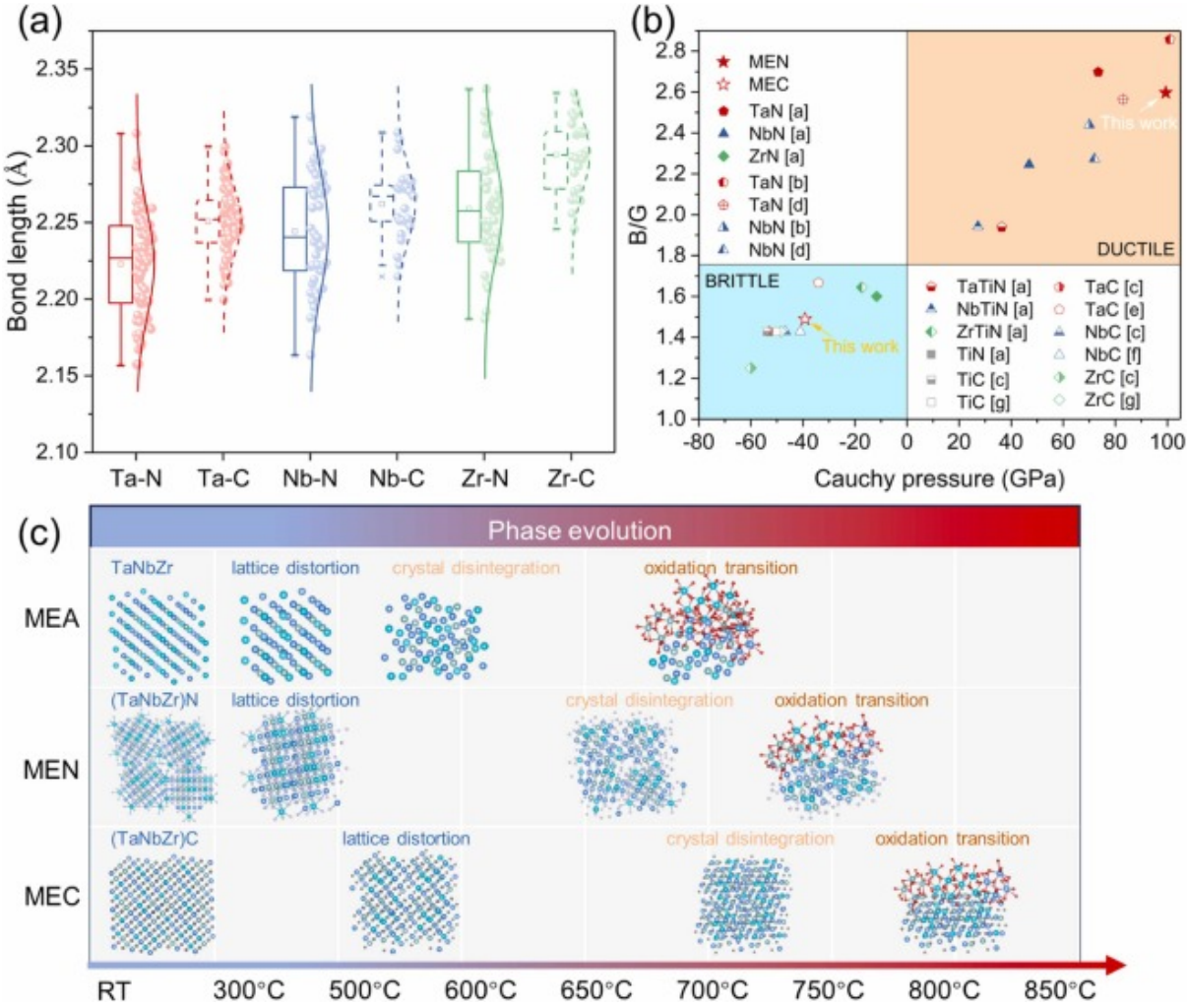

1. Download: Download high-res image (517KB)
2. Download: Download full-size image

Fig. 11. (a) Distribution of metal-nonmetal bond length in MEN and MEC, (b) The B/G vs. Cauchy pressure map of quaternary MEN and MEC. (c) Phase transition diagrams of the coatings at different temperatures based on the results of in-situ XRD. Ref. a [57], b [60], c [61], d [62], e [63], f [64], g [65].

In addition, the intrinsic brittle-ductile behavior of materials is crucial in engineering applications, often assessed through multiple indicators such as the B/G ratio and Cauchy pressure, to predict this behavior [53]. Generally, larger B/G values (>1.75) indicate ductility, while smaller B/G values imply greater brittleness in materials [54]. Cauchy pressure (C_{12}-C_{44}) [55] can characterize the bonding characteristics of materials: positive Cauchy pressure values indicate predominance of metallic bonding, demonstrating ductility, whereas negative values suggest dominance of covalent bonding, indicating greater brittleness. Computational and associated research results (Fig. 11b) reveal that MEN has a B/G value greater than 1.75, with a positive Cauchy pressure value, while MEC exhibits the opposite trend. This indicates that the MEN system possesses good ductility, whereas the MEC system is brittle.

4.2. Phase evolution and high temperature stability of quaternary ceramic

Based on the preceding in-situ XRD results, it is evident that as the temperature rises, none of the

three coatings exhibit the formation of intermediate phases before the emergence of medium entropy oxides (MEO, which could also be mixed oxides). Fig. 11c illustrates a schematic of the comprehensive phase composition and phase evolution obtained from in-situ XRD testing. When the temperature is below 500 °C, the diffraction peaks of MEN and MEA coatings shift towards lower angles, while the diffraction peaks of MEC remain relatively fixed. This observation is attributed to the recrystallization behavior occurring with the increasing temperature in the partially amorphous phases present in the as-deposited coatings [66]. As discussed earlier regarding the surface XRD diffraction spectra of as-deposited coatings and the thermodynamic properties of crystal structures, the as-deposited MEN coating exhibits only one prominent high-intensity peak at around 59° with broad diffraction peaks at lower angles, indicating the presence of a certain amount of amorphous phase. With increasing temperature, the amorphous and crystalline phases gradually transition to more stable crystal structures through lattice distortion. With temperature elevation, the phase structure of the MEA coating undergoes a transformation from lattice relaxation and lattice distortion, with the peak intensity gradually decreasing and the width increasing, eventually transitioning to an amorphous structure. This evolution process continues until 700 °C for the MEN coating, 750 °C for the MEC coating, and 650 °C for the MEA coating. The evolution of the amorphous structure is decomposed from a randomly disordered atomic arrangement, typically exhibiting excellent corrosion resistance and high-temperature stability, albeit potentially sacrificing some mechanical properties [67]. As the temperature further increases, distinct new phases are detected on the surface of the coatings, although relatively weak diffraction peaks still remain at the positions of the original phases.

The onset temperature for the formation of oxide phases in the MEA coating is 700 °C, sequentially lower than that of the MEN and MEC coatings. This is consistent with the lower activation energy observed in experimental results, indicating that MEA is more prone to structural disintegration. The high-temperature oxidation curves of the quaternary ceramic coatings in this study follow a parabolic pattern, indicating that oxygen diffuses through the oxide layer during the oxidation process. Therefore, the antioxidative properties of the coatings are closely related to the formation and evolution of the oxide layer in the environment. The worm-like and porous microstructures on the surfaces of MEN and MEC at high temperatures facilitate the internal diffusion of oxygen, hindering the formation of dense oxide layers. Although various indicators suggest that MEC exhibits higher high-temperature thermal stability, the application of coatings requires consideration not only of the properties of the coatings themselves but also of the performance at the coating-substrate interface. Considering the thermodynamic properties of the coating structure, the brittle MEC coating is more prone to interlayer cracking or fragmentation during thermal cycling processes due to mismatched residual thermal stresses and thermal expansion coefficients. MEN, which exhibits better experimental results and better adhesion to the substrate, presents a balanced choice.

5. Conclusions

Quaternary ceramic coatings were prepared using a double glow plasma surface alloying technique and investigated the impact of introducing N and C atoms into TaNbZr metallic coatings on their high-temperature performance and stability through high-temperature cyclic oxidation tests, in-situ X-ray diffraction, and density functional theory calculations. Several key results and observations can be summarized as follows:

- (1)

The prepared quaternary ceramic coatings possess metallurgical transition layers similar to metallic

coatings, and the growth of these coatings exhibits pronounced structural orientation.

- (2)

MEC and MEN quaternary ceramic coatings exhibit superior antioxidation properties compared to TaNbZr metallic coatings in cyclic oxidation tests indicate. This superiority is manifested by a thermal weight gain of only 30 %-60 % within 100 hours (10 cycles). Among them, the MEN coating maintains a relatively intact protective layer even at 800 °C.

- (3)

In-situ XRD tests demonstrate the high-temperature stability of MEC and MEN coatings in hot air, with both coatings remaining phase stable at 750 °C and 700 °C, respectively, without the emergence of new phases. This is a great improvement compared to the obvious structural disintegration of the MEA coating after 550 °C.

- (4)

Base on ab initio calculations and a quasi-harmonic Debye-Grüneisen model, the higher thermal expansion coefficients and thermal pressures of MEN and MEC. Therefore, an intermediate transition metal layer with similar thermal expansion coefficients and lower thermal pressures benefit in enhancing the adhesion between ceramic coating and matrix. Furthermore, MEN and MEC exhibit higher high-temperature bulk moduli, similar high-temperature softening behaviors, and higher specific heat capacities, implying that quaternary ceramic coatings have enhanced high-temperature strength and thermal stability in environments characterized by significant temperature fluctuations.

- (5)

Combining the findings from previous studies, the quaternary ceramic coatings, particularly (TaNbZr)N, demonstrate exceptional mechanical properties and high-temperature stability, making them promising candidates for extreme environment applications.

CRediT authorship contribution statement

Haiyang Yu: Conceptualization, Data curation, Investigation, Methodology, Writing – original draft, Writing – review & editing. **Wenping Liang:** Conceptualization, Data curation, Funding acquisition, Investigation, Methodology, Project administration, Resources, Supervision, Writing – review & editing. **Qiang Miao:** Conceptualization, Data curation, Funding acquisition, Investigation, Methodology, Project administration, Resources, Supervision, Writing – review & editing. **Mengjuan Yin:** Resources, Data curation, Validation, Visualization, Writing – review & editing. **Yong Wang:** Resources, Data curation, Validation, Visualization, Writing – review & editing. **Hongfei Liu:** Resources, Supervision, Validation, Visualization, Writing – review & editing. **Hongmei Jin:** Resources, Software, Data analysis, Validation, Visualization, Writing – review & editing. **Fengxia Wei:** Resources, Data analysis, Visualization, Writing – review & editing. **Na Gong:** Conceptualization, Data curation, Funding acquisition, Investigation, Methodology, Project administration, Resources, Supervision, Writing – review & editing.

Declaration of Competing Interest

The authors declare that they have no known competing financial interests or personal relationships that could have appeared to influence the work reported in this paper

Acknowledgement

This work is supported by the National Major Science and Technology Projects of China (Y2022-III-0004-0013), the National Natural Science foundation of China (No. 52272065) and the Fundamental Research Funds for the Central Universities (NO. NP2022424). H. Yu gratefully acknowledge financial support from Nanjing University of Aeronautics and Astronautics PhD short-term visiting scholar

project (No. 230305DF06) and China Scholarship Council. N. Gong appreciates the support from the Structural Metal Alloy Program (SMAP), Grant No. A18B1b0061, and Manufacturing of Multi-Material Net-Shape Parts with Heterogeneous Properties (MMNH), Grant No. M22K5a0045 in A*STAR.